


## ORIGINAL ARTICLE

# Bifocal 532/1064 nm alternately illuminated photoacoustic microscopy for capturing deep vascular morphology in human skin

Z. Wang,<sup>1,2</sup>  F. Yang,<sup>1,2</sup> H. Ma,<sup>1,2</sup> Z. Cheng,<sup>1,2</sup> W. Zhang,<sup>1,2</sup> K. Xiong,<sup>1,2</sup> T. Shen,<sup>3</sup> S. Yang<sup>1,2,\*</sup>

<sup>1</sup>MOE Key Laboratory of Laser Life Science and Institute of Laser Life Science, College of Biophotonics, South China Normal University, Guangzhou, China

<sup>2</sup>Guangdong Provincial Key Laboratory of Laser Life Science, College of Biophotonics, South China Normal University, Guangzhou, China

<sup>3</sup>Department of Plastic and Aesthetic Surgery, Nanfang Hospital, Southern Medical University, Guangzhou, China

\*Correspondence: S. Yang. E-mail: yangsh@scnu.edu.cn

## Abstract

**Background** As a promising technology, photoacoustic microscopy (PAM) plays a critical role in diagnosis and assessment of dermatological conditions by providing subtle vascular networks non-invasively. However, the established PAMs are insufficient for clinical dermatology when faced with complex structures of human skin instead of animal models owing to high melanin content and superimposed vasculature for Asians, which cannot balance the spatial resolution and the imaging depth.

**Objectives** To evaluate the ability of bifocal 532/1064-nm alternately illuminated photoacoustic microscopy (BF-PAM) to non-invasively reveal the morphological structure of human skin for improving the diagnosis and therapeutic efficacy of skin diseases.

**Methods** A BF-PAM was developed to capture biopsy-like information of human skin from epidermis to hypodermis. The optical foci of the two excitation beams are staggered in the axial direction to form an extended depth-of-field, which can maintain the lateral resolution and the contrast of PA image.

**Results** The imaging capability of the BF-PAM was demonstrated by depicting the vascular morphology of multilayered skin with imaging depth of ~3 mm. Furtherly, vascular malformations in port-wine stains skin were quantitatively assessed without the need for any contrast agent, and the distribution, depth and diameter of the ectatic vessels can determine an optimal treatment protocol for port-wine stains lesions.

**Conclusions** The quantitative vascular morphology in the dermis can be used to accurately assess vascular characteristics, in which case it enables clinicians to determine optimum treatment parameters in individual patients. As a non-invasive imaging technique, BF-PAM holds great potential to provide objective assessment to enhance the therapeutic efficacy.

**Ethical statement** The study was conducted in accordance with the Declaration of Helsinki (as revised in 2013). The study was approved by the Chinese Ethics Committee of Registering Clinical Trials (ChiECRCT20200184) and registered with Chinese Clinical Trial Registry (ChiCTR2000034400). Before skin imaging, written informed consent was taken from all individual participants.

Received: 5 July 2021; Accepted: 26 August 2021

## Conflicts of interest

All authors have completed the ICMJE uniform disclosure form. The authors have no conflicts of interest to declare.

## Funding sources

National Natural Science Foundation of China (61822505; 11774101; 61627827), the Science and Technology Planning Project of Guangdong Province, China (2015B020233016) and the Science and Technology Program of Guangzhou (2019050001).

## Introduction

Photoacoustic imaging (PAI), has been proposed as an emerging medical imaging technology,<sup>1–6</sup> which holds promise for a wide range of biomedical applications by creating multiscale multiparameter images *in vivo* ranging from organelles to organs.<sup>7</sup> As a meritorious application mode of PAI, PAM can capture morphological, functional and molecular information of biological tissue for high-resolution and non-invasive imaging.<sup>8–12</sup> In basic biomedical research, the morphological and functional information of vascular morphology in animal models can be easily acquired through PAM,<sup>13–18</sup> which takes advantage of the endogenous haemoglobin without any contrast agent. Furthermore, as a new detection approach, PAM was gradually proposed and developed in dermatology to non-invasively visualize pigmentation and vasculopathy for human skin,<sup>19–23</sup> such as quantification reveals psoriasis, port wine stain (PWS) and atopic dermatitis,<sup>24–27</sup> which can be helpful in early diagnosis and precision therapy. In comparison with conventional optical microscopy, PAM has superior imaging depth, which has exceeded the soft-depth limit in human skin, and it holds great promise to break through the hard-depth limit with deep penetration and high contrast.<sup>28</sup> However, there is still no PAM system to achieve full-structure imaging of human skin. In order to achieve a deeper imaging depth, some photoacoustic tomography systems using near-infrared laser have been developed for tumour detection,<sup>29,30</sup> but the microvascular structures of human skin cannot be revealed due to the limited resolution. As an important theory, the interaction between light and biological tissues needs to be well understood to optimize and develop the PAM system. The light propagation inside the biological tissue is characterized by strong scattering and absorption,<sup>31,32</sup> which determine the imaging quality of the PAM system. The difference is that PAM is absorption-based imaging, and scattering is a controllable factor in the PAM system that can be adjusted by laser wavelength to enhance imaging depth and maintain the lateral resolution at deeper tissue.<sup>33</sup> Since the scattering and absorption coefficient of human skin vary at different wavelengths,<sup>34,35</sup> different laser-equipped PAM systems have different imaging performance. For the conventional PAM systems, laser within the visible (VIS) light is generally equipped to image the vascular network,<sup>14–17</sup> where the haemoglobin has good responsiveness and high detection sensitivity.<sup>33</sup> However, the surrounding biological tissues also have strong scattering in the VIS window, leading to poor imaging depth, which makes the conventional PAM limited to visualizing superficial skin features. Moreover, the human skin presents multilayered structures and a complex heterogeneous medium, where the blood and pigment content are spatially distributed variably in depth.<sup>36</sup> Therefore, it is difficult for the laser beam in VIS window to penetrate the total human skin thickness. To acquire deep penetration depth and high optical resolution, Wang *et al.* proposed near-infrared optical-resolution

photoacoustic microscopy (NIR-OR-PAM),<sup>37</sup> which obtained penetration depth of 3.2 mm in chicken breast tissue *ex vivo* with high-resolution. Gradually, near-infrared light or multiple wavelengths were used in PAM to increase the imaging depth or identify different absorbers, such as melanin or nanoprobe.<sup>38–42</sup> However, these systems are mainly used for basic medical research on small animals rather than for human research. There is a great need to develop a specialized PAM system for dermatology, which can investigate the fine morphological structures of human skin from epidermis to hypodermis with high resolution and deep penetration.

Here, according to the anatomical structures and optical characteristics of the human skin, a bifocal photoacoustic microscopy (BF-PAM) system was developed by combining the 532-nm laser and 1064-nm laser as the excitation lights for visualizing the subtle vascular morphology from epidermis to hypodermis. The BF-PAM was developed to address the limitations of visible-light shallow penetration depth and short focal zone in conventional OR-PAM. The imaging results demonstrate that BF-PAM has the potential to non-invasively obtain more biopsy-like information on human skin, which is more effective in the clinical study and dermatopathology.

## Materials and methods

Tuchin *et al.*<sup>31</sup> confirmed that the wavelength with the deepest penetration is 1090 nm in biological tissues. Considering the absorption spectrum of haemoglobin and the convenience of the pulsed laser equipment, 532-nm laser in VIS window and 1064-nm laser in NIR window were selected as the excitation lights. Figure 1a graphically illustrates the laser excitation and the image reconstruction of BF-PAM system. Two laser beams are used to irradiate the skin and the PA images are reconstructed through the depth-resolved signals. The 532-nm laser beam focuses on the epidermis and the superficial dermis, while the 1064-nm laser beam focuses on the deep dermis. The optical focus of the two excitation beams are staggered in the axial direction to form the extended depth of field, which can maintain the lateral resolution and image contrast in deeper tissues. For BF-PAM system, each laser pulse produces a one-dimensional (1D) depth-resolved Aline signal, and two laser beams were triggered alternately with a 50- $\mu$ s delay. 2D transverse scanning obtains a 3D data, and the scanning speed is 10 mm/s. The step size of the X axis is 8  $\mu$ m, and the step size of the Y axis is 10  $\mu$ m. The laser pulse repetition rate is 10 kHz. At last, the epidermis and superficial dermis were reconstructed by 532-nm excited PA signals, while the deep dermis and hypodermis was reconstructed by 1064-nm excited PA signals. Monte Carlo simulation for light propagation in tissue is the gold standard for studying the light propagation in biological tissue.<sup>43</sup> The propagation characteristics of light in air and the simulated biological skin were simulated by Monte Carlo. The spots of 532-nm and 1064-nm lasers at different depths in the simulated

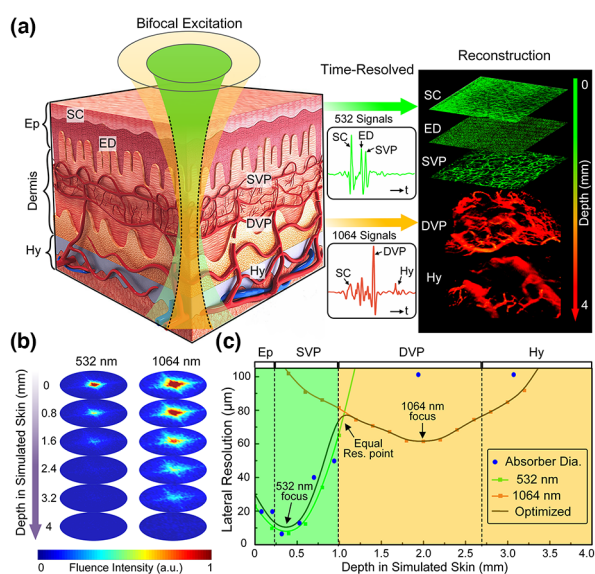


**Figure 1** Bifocal photoacoustic microscopy system using two excitation beams. (a) The schematic for the dual-wavelength laser excitation and photoacoustic image reconstruction of BF-PAM. (b) The simulated transmission optical intensity map of 532 nm laser and 1064-nm laser beams at different depths in the simulated skin. (c) The lateral resolution varies with the depth in the simulated skin and the diameters of main absorbers of the human skin in different skin layers. Ep, epidermis; Hy, hypodermis; SC, stratum corneum; SB, stratum basale; ED, epidermal-dermal junction layer; SVP, superficial vascular plexus; DVP, deep vascular plexus.

biological skin are shown in Fig. 1b. The results show that the penetration depth of the 532-nm laser can reach  $\sim 800$   $\mu\text{m}$  and the 1064-nm laser can reach  $\sim 3$  mm, which is basically consistent with the results calculated by the diffusion theory. Through the simulated excitation laser beams, the relationship between the lateral resolution and imaging depth is demonstrated in Fig. 1c, showing that BF-PAM system maintains good lateral resolution in deep tissues. The diameters of endogenous absorbers at different depths in the skin tissue are also shown in Fig. 1c, indicating that the system can reveal endogenous absorbers with high resolution. In the BF-PAM system, 532-nm laser was used to visualize the fine structures of the epidermis and the capillary network in the superficial dermis, and 1064-nm laser was used to detect the nutrient vessels in the deep dermis and hypodermis. The BF-PAM system is capable of imaging the endogenous absorbers in each layer of the human skin.

The schematic diagram of the BF-PAM system (SDPM-510, Guangdong Photoacoustic Medical Technology Co.,Ltd) is shown in Fig. 2a. The BF-PAM system employs two nanosecond laser systems operating at 532 nm (DTL-314QT, Laser-export) and 1064 nm (DTL-324QT, Laser-export) with  $\sim 7$  ns pulse width. Both laser beams are attenuated, spatially filtered and coupled to the optical fibres as excitation sources. For 532-nm

laser, the laser beam is cleaned by a spatial filter system (KT310/M, Thorlabs), which passes through a 10- $\mu\text{m}$ -diameter pinhole for spatial filtering, and then coupled into a single-mode fibre using a fibre coupler (PAF-X-7-A, Thorlabs). For 1064-nm laser, the laser beam is also spatially filtered by a 50- $\mu\text{m}$ -diameter pinhole, and then coupled into a multimode fibre using a fibre coupler (PAF-X-7-C, Thorlabs). For simultaneous imaging, two laser devices are triggered alternately by the field programmable gate array (FPGA) to produce PA signals. The fibres guide the laser beams into a 2D-scanner (LS2-25T, Jiancheng Optics) probe. The internal optical path of the integrated BF-PAM probe is shown in Fig. 2b, where the laser beams are collimated and focused respectively, and then converged by a dichroic mirror (DMSP650, Thorlabs). The 532-nm and 1064-nm laser foci are configured coaxially and adjusted at different depths. The distance between 532 focus and 1064 focus is about 1.5 mm. A focused ringed transducer (Central frequency: 30 MHz, Doppler Inc.) with a focal length of 8 mm is used to receive the PA signals. The acoustic focus is set at the geometric centre of the two optical foci to guarantee the best receiving sensitivity. The received signals are amplified (LNA-650, RF Bay) and digitized with a data acquisition card (M3i.3221, Spectrum) at the sampling rate of 200 MS/s. To characterize the spatial resolution of BF-PAM system, two laser sources were separately used to alternately illuminate the sample. A sharp-edged surgical blade was scanned along the same edge with 1- $\mu\text{m}$  step size. The system was operated at only 532-nm laser radiation to calculate the 532-imaging resolution. As shown in Fig. 2c, using edge spread function (ESF), the data along the edge of the maximum amplitude projection (MAP) image (inset in Fig. 2c) were fitted. The lateral resolution (532 nm laser) determined from the line-spread function (LSF) was 6.6  $\mu\text{m}$ . Similarly, the system was operated at only 1064 nm laser radiation to calculate the 1064-imaging resolution. The lateral resolution of the BF-PAM was characterized using carbon fibre in Fig. 2d. The calculated lateral resolution (1064-nm laser) from the full width at half maximum (FWHM) of the fitted data was 46.8  $\mu\text{m}$ . The axial resolution is determined by the acoustic bandwidth of the transducer, and thus, BF-PAM share the same axial resolution regardless of the laser excitation. The envelope of the photoacoustic A-line signal from the carbon fibre in Fig. 2e indicates that the axial resolution is 50.6  $\mu\text{m}$ .

## Results

The skin tissue of the adult SD rat with multilayered anatomical structures, which is a good model for studying the human skin tissue. Before the experiments, the rat was injected with sodium pentobarbital (30 mg/kg) to keep motionless and the hair was removed with depilatory cream. The rat was placed on a heating pad on the fixed stage to maintain the body temperature during the experiment. Ultrasound gel and deionized water were used to couple the PA signals between the rat skin and the transducer.

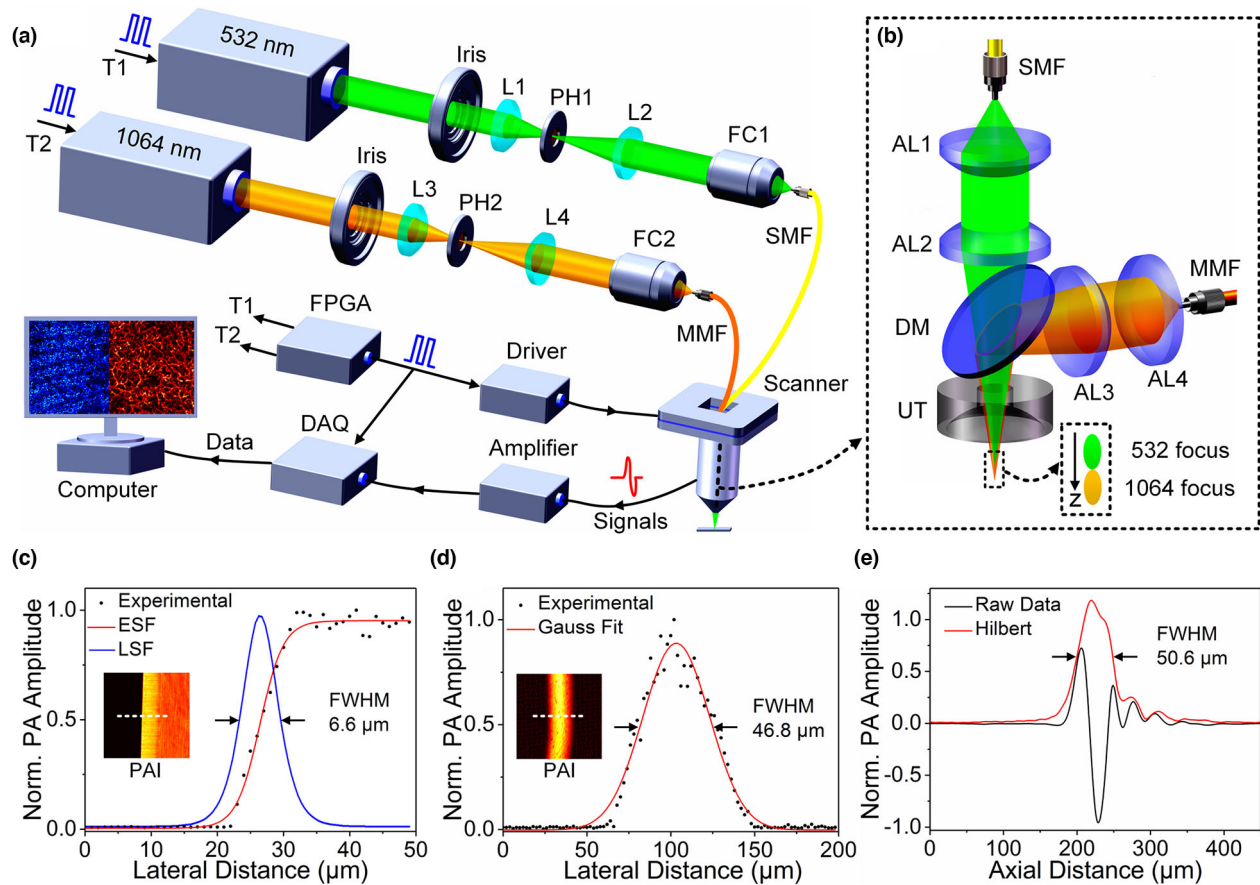


**Figure 2** Schematic diagram and spatial resolution of the BF-PAM system. (a) Optical paths and electrical connections of system. (b) The internal optical path of the integrated BF-PAM probe. The 532 and 1064 foci were configured coaxially but at different depth. (c) The measured lateral resolution of the 532 nm PA imaging by sharp-edged blade method. (d) The lateral resolution of the 1064 nm PA imaging by carbon fibres. (e) The axial resolution of microscope. L1-L4, convex lenses; PH1, PH2, pinhole; FC1, FC2, fibre coupler; SMF, single-mode fibre; MMF, multimode fibre; DAQ, data acquisition unit; FPGA, field programmable gate array; T1, T2, trigger; AL1-AL4, aspherical lens; DM, dichroic mirror; UT, ultrasonic transducer.

The dorsal skin of the rat was imaged in Fig. 3 to demonstrate the imaging capability of our BF-PAM system for skin tissue. The depth-encoded horizontal-sectional images are shown in Fig. 3a,b. Figure 3a was reconstructed by the 532 nm-excitation signals and Fig. 3b was reconstructed by 1064-nm excitation signals. The results show the 532 nm laser can reveal capillary networks with high resolution while 1064 nm laser in BF-PAM system has poor resolution for superficial microvasculature but can detect deeper vessels. After the experiment is completed, the mouse is euthanized, and then the skin of the imaging area is selected for hematoxylin and eosin (H&E) histopathology. As shown in Fig. 3c, the structures of the epidermis, dermis and hypodermis can be clearly distinguished in the H&E stained image, and it can be observed that epidermis and dermis contain abundant capillary networks, while the muscle layer and sub-muscular tissue have large diameter vessels. Figure 3d,e show

the x-z cross-sectional MAP images of the rat back corresponding to Fig. 3a,b, respectively. As shown in Fig. 3f, the merged PA cross-sectional image can reveal the entire skin tissue from the epidermis to the submuscular tissue, which is basically consistent with the H&E histopathology in the depth direction. This experiment indicates that BF-PAM holds the potential for non-invasively studying the relationship between abnormal expansion of skin vascular network and deep tissue vessels in rat models.

To investigate the BF-PAM ability to reveal the anatomical structures of different skin layers, we performed imaging at the human palm. The skin conditions of the volunteers were evaluated by the experienced dermatologist. The pulsed laser illumination energy of 12 mJ/cm<sup>2</sup> at 532 nm and 60 mJ/cm<sup>2</sup> at 1064 nm was less than the ANSI safety limit.<sup>44</sup> Figure 4a shows cross-sectional image obtained only 532-nm laser excitation,

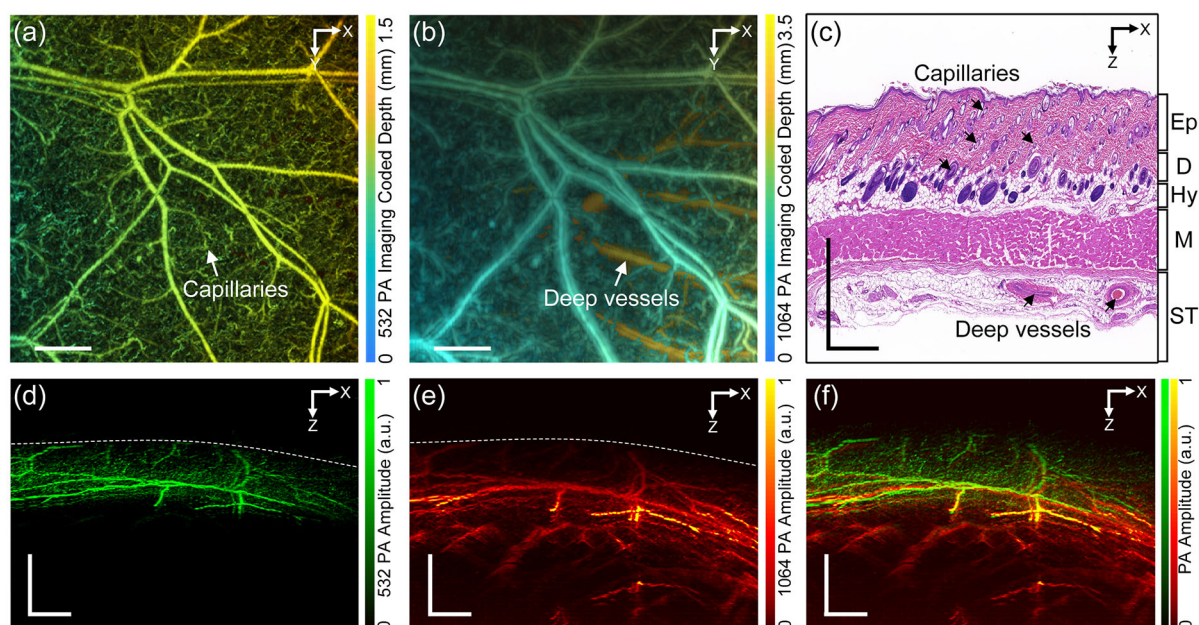


**Figure 3** In vivo imaging of dorsal skin of the adult SD rat. (a) The depth-coded horizontal-sectional image reconstructed from 532 nm-excitation signals. (b) The depth-coded horizontal-sectional image reconstructed from 1064 nm-excitation signals. (c) Image with hematoxylin and eosin (H&E) histopathology. (d) The 532 nm PA cross-sectional MAP image of the dorsal skin. (e) The 1064 nm PA cross-sectional MAP image of the dorsal skin. (f) The merged PA cross-sectional MAP image. Ep, epidermis; D, dermis; Hy, hypodermis; M, muscles; ST, submuscular tissue. Scale bar: 1 mm.

while Fig. 4b shows cross-sectional image obtained only 1064-nm laser excitation. Comparing the two cross-sectional images, Fig. 4a has higher resolution and contrast to reveal superficial tissues, while Fig. 4b has deeper penetration to detect deep tissues. Figure 4c is the merged 3D reconstruction image by 532 nm-excitation signals and 1064 nm-excitation signals. The imaging result shows the abundant microvasculature in dermis and hypodermis and the vessel diameter increases with depth. Figure 4d–f show the MAP image in the direction perpendicular to the skin surface within the depth ranges marked in Fig. 4a. As shown in Fig. 4d, the lateral MAP image of stratum corneum is depicted. The system yields higher resolution images with a skin texture trait. Figure 4e shows the MAP image correspond to the epidermal-dermal junction layer. In this layer, the capillary loops are visualized as regular parallel curves. The zoom in Fig. 4e shows single capillary loop located 100–250  $\mu\text{m}$  below the surface. Compared with the epidermis, which contains a lot of pigment, the dermis is rich in vascular network. As shown in Fig. 4f, the abundant microvasculature locates in the superficial reticular layer (250–720  $\mu\text{m}$  below the surface), of which morphological structures are obviously different with epidermis. Furtherly, Fig. 4g,h show the MAP image acquired from Fig. 4b in the deep reticular layer and hypodermis. The blood vessels in Fig. 4g have a diameter of 60–380  $\mu\text{m}$  and located 720–1800  $\mu\text{m}$

below the skin surface. Meantime, the deep arteriovenous plexus of the dermis and hypodermis (1800–3000  $\mu\text{m}$  below the skin surface) shown in Fig. 4h. Finally, Fig. 4i shows a merged image of the vascular network located in the dermis and hypodermis, and the morphology of the microvasculature are proved to affect the human skin physiological status. The imaging experiments demonstrated the ability of the BF-PAM to reveal the morphological structures of multilayered skin *in vivo*.

Finally, the anatomical structures of normal and PWS skin were investigated non-invasive by BF-PAM system. It is useful for the diagnosis and photodynamic therapy of the PWS to reveal the pathological changes of each skin layers in the lesion region. PWS skin is caused by a malformed dilatation of the capillaries. Conventional dermoscopic technique is difficult to penetrate the superficial skin due to the large amount of haemoglobin increase in the superficial skin. Our previous system equipped with a single 532 nm laser can only reveal the superficial layers of the dermis,<sup>23,25,26</sup> but this cannot provide enough information for the diagnosis and treatment of the PWS skin. Here, *in vivo* imaging of normal skin and PWS skin using BF-PAM are shown in Fig. 5. The epidermal layer (Fig. 5a,e) and superficial dermal layer (Fig. 5b,f) were reconstructed by 532-nm excitation signals, while the deep dermal layer (Fig. 5c, g) was reconstructed by 1064-nm excitation signals. Further,

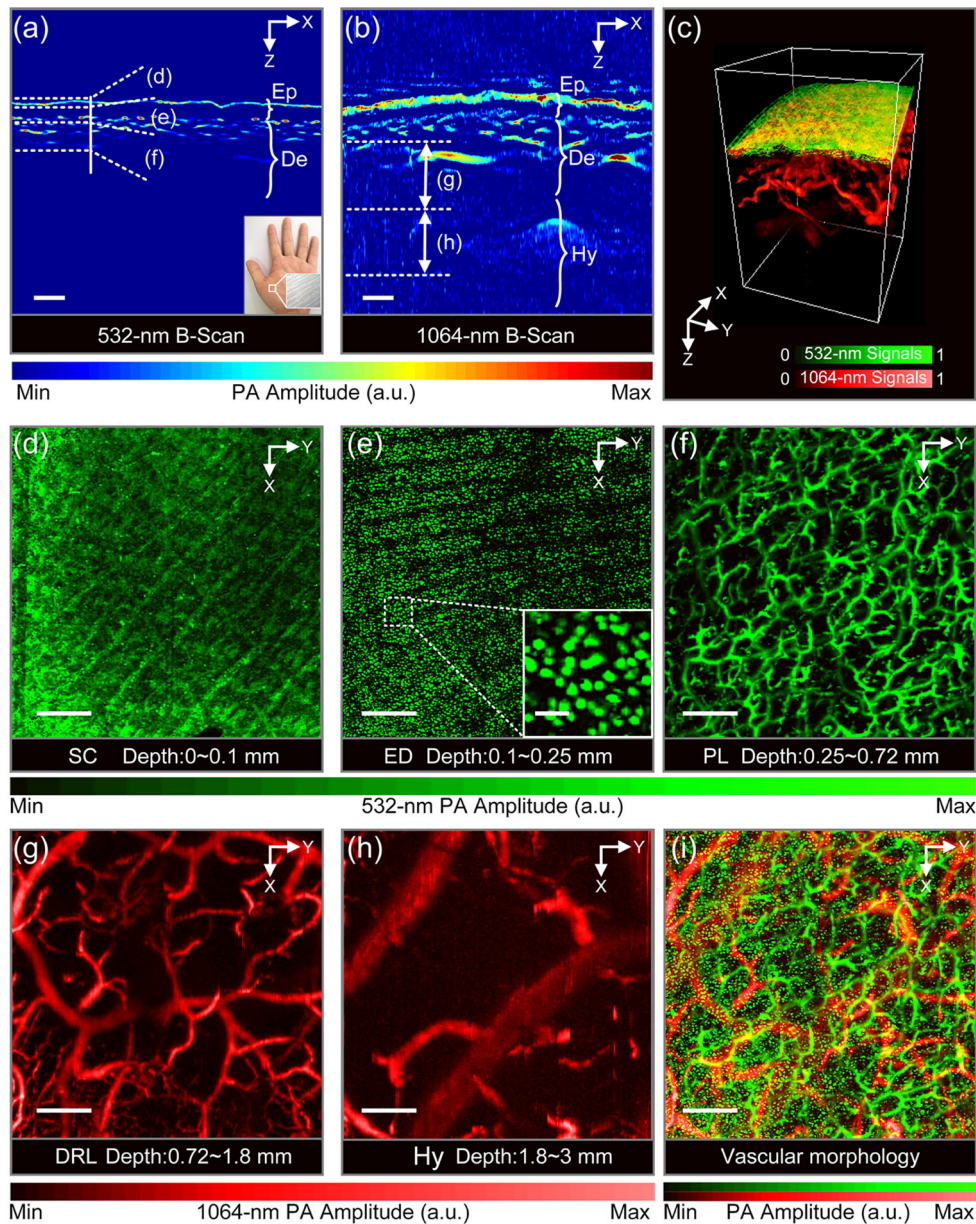


**Figure 4** In vivo imaging of the human palm. (a) A cross-sectional 532 nm PA imaging of the human palm. Photograph of the palm from which the in vivo data was acquired, the white frame is the imaging area. Scale bar: 500  $\mu\text{m}$ . (b) A cross-sectional 1064 nm PA imaging of the human palm. Scale bar: 500  $\mu\text{m}$ . (c) The merged 3D reconstruction image. (d–f) PA lateral MAP images of skin layers at different depths, acquired from 532 nm PA imaging. Scale bar: 1 mm. In (e) a zoom in into the region marked by the white dashed box is shown. Scale bar: 0.1 mm. (g–h) PA lateral MAP images of skin layers at different depths, acquired from 1064 nm PA imaging. Scale bar: 1 mm. (i) The merged vascular morphology in the dermis and the hypodermis. Ep, epidermis; De, dermis; SC, stratum corneum; ED, epidermal-dermal junction layer; PL, papillary layer; DRL, deep reticular layer; Hy, hypodermis.

Fig. 5d,h show the merged images of the vascular morphology of normal skin and PWS skin, respectively. As shown in Fig. 5a, e, the texture and structures of the skin can be observed with high resolution in the epidermis. The pigment density in the

PWS skin is slightly lower than that in normal skin because of the abnormal expansion of blood vessels in the dermis. Comparing the superficial dermal layer of PWS skin with that of normal skin, the vascular networks in the PWS skin were severely

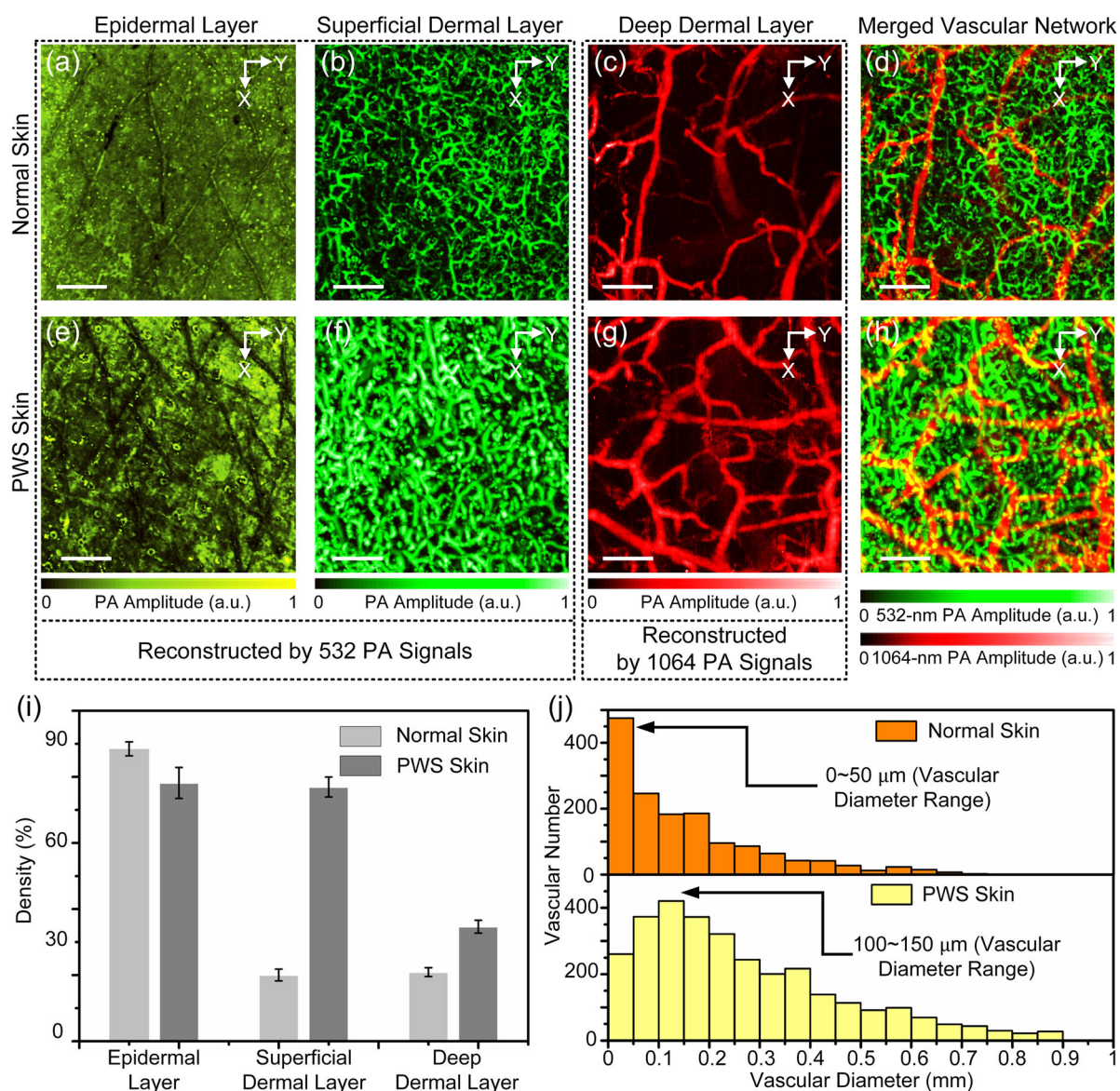


**Figure 5** In vivo imaging of normal skin and PWS skin. (a–c) PA lateral MAP image of epidermal layer, superficial dermal layer and deep dermal layer of normal skin. Scale bar: 1 mm. (d) Merged vascular network of normal skin. Scale bar: 1 mm. (e–g) PA lateral MAP image of epidermal layer, superficial dermal layer and deep dermal layer of PWS skin. Scale bar: 1 mm. (h) Merged vascular network of PWS skin. Scale bar: 1 mm. (i) Statistics of vascular density in the dermis layer of PWS skin and normal skin. (j) Statistics of vascular number and vascular diameter in the superficial dermis layer of PWS skin and normal skin.

deformed and dilated, and the density and diameter of vessels were significantly higher than that of normal skin. Further, the vascular networks in the deep dermal layer are visualized by 1064 nm laser. The blood vessels in the deep dermal layer have more branches with a diameter of 40–500  $\mu\text{m}$  to provide nutrition to the superficial dermis. As shown in Fig. 5i, the vascular density in PWS skin increases about four times in the superficial

dermis. To further quantitatively investigate the vascular changes in the superficial layer. Here, the vertical line passing through the vascular skeleton intersects the vascular boundary at two points, and the distance between these two points is defined as the diameter of the vessel at that point. Figure 5j shows that the diameter and number of blood vessels in the superficial dermis of PWS skin is mainly distributed in 100–150  $\mu\text{m}$ , while the

diameter of blood vessels in normal skin is mainly distributed in 0–50  $\mu\text{m}$ . There is an abnormal dilatation of the diameter of the blood vessels in the PWS skin. The imaging results show that the BF-PAM system can provide auxiliary information for the diagnosis and treatment of the PWS skin.

## Discussion

Herein, we report on the development of BF-PAM as a new method to overcome the limitations in imaging depth of conventional PAM techniques. The conventional PAM is limited by the short focal zone and shallow penetration depth in human skin, which can only visualize superficial skin features. The proposed BF-PAM system, combining the VIS and NIR laser as the excitation sources to form the extended depth of field, which can reveal the subtle skin morphology from epidermis to hypodermis. The new approach has been shown to accurately depict the complex anatomical structures in each layer of the skin within a depth of 3 mm, and realize non-invasively PA biopsy of the full-structure skin. The imaging results of PWS skin show that the microscope can visualize the fine anatomical structures of different layers of human skin and monitor the changes of pigment in epidermis and vascular morphology in dermis. Overall, BF-PAM has high clinical potential in quantitative analysis, local monitoring and treatment scheduling for skin diseases. Some performance needs to be enhanced before the BF-PAM can be considered for clinical application of dermatology and dermoscopy. Primarily, motion artefacts might occur if the imaging speed is slow, especially in the slow-scanning axis. A motion correction algorithm was used to eliminate the effects of motion on the image to ensure accurate structural images for diagnosis.<sup>45</sup> Secondly, we have been constantly working hard to upgrade our system, and a MEMS scanner based OR-PAM with faster scanning speed and smaller size is on its way. Additionally, the oxygen saturation and precise distinction of endogenous pigments can be resolved by algorithm. Finally, reliable and compact LD or LED devices for multi-wavelength excitation will reduce costs and enhance image quality. We look forward to seeing the wide application of PAM in dermatology.

## Acknowledgements

The patients in this manuscript have given written informed consent to publication of their case details.

## References

- Liopo A, Su R, Oraevsky AA. Melanin nanoparticles as a novel contrast agent for photoacoustic tomography. *Photoacoustics* 2015; **3**: 35–43.
- Chen R, Huang S, Lin T *et al*. Photoacoustic molecular imaging-escorted adipose photodynamic-browning synergy for fighting obesity with virus-like complexes. *Nat Nanotechnol* 2021; **16**: 455–465.
- Lv J, Xu Y, Xu L, Nie L. Quantitative functional evaluation of liver fibrosis in mice with dynamic contrast-enhanced photoacoustic imaging. *Radiology* 2021; **300**: 204134.
- Li W, Sun X, Wang YU *et al*. *In vivo* quantitative photoacoustic microscopy of gold nanostar kinetics in mouse organs. *Biomed Opt Express* 2014; **5**: 2679–2685.
- Park B, Bang CH, Lee C *et al*. 3D wide-field multispectral photoacoustic imaging of human melanomas *in vivo*: a pilot study. *J Eur Acad Dermatol* 2021; **35**: 669–676.
- Erfanzadeh M, Zhu Q. Photoacoustic imaging with low-cost sources. A Review. *Photoacoustics* 2019; **14**: 1–11.
- Wang LV, Hu S. Photoacoustic tomography: *in vivo* imaging from organelles to organs. *Science* 2012; **335**: 1458–1462.
- Chen Q, Qin W, Qi W, Xi L. Progress of clinical translation of handheld and semi-handheld photoacoustic imaging[J]. *Photoacoustics* 2021; **22**: 100264.
- Qin W, Gan QI, Yang L *et al*. High-resolution *in vivo* imaging of rhesus cerebral cortex with ultrafast portable photoacoustic microscopy. *NeuroImage* 2021; **238**: 118260.
- Wang Y, Liang G, Liu F, Chen Q, Xi L. A long-term cranial window for high-resolution Photoacoustic imaging[J]. *IEEE Trans Biomed Eng* 2020; **68**: 706–711.
- Bi R, Dinsh US, Goh CC *et al*. *In vivo* label-free functional photoacoustic monitoring of ischemic reperfusion. *J Biophotonics* 2019; **12**: e201800454.
- Rao B, Leng X, Zeng Y *et al*. Optical resolution photoacoustic microscopy of ovary and fallopian tube. *Sci Rep* 2019; **9**: 1–9.
- Cho S, Baik J, Managuli R *et al*. 3D PHOVIS: 3D photoacoustic visualization studio. *Photoacoustics* 2020; **18**: 100168.
- Chen Q, Guo H, Jin T *et al*. Ultracompact high-resolution photoacoustic microscopy. *Opt Lett* 2018; **43**: 1615–1618.
- Yao J, Wang L, Yang J-M *et al*. High-speed label-free functional photoacoustic microscopy of mouse brain in action. *Nat Methods* 2015; **12**: 407–410.
- Yang F, Wang Z, Zhang W *et al*. Wide-field monitoring and real-time local recording of microvascular networks on small animals with a dual-raster-scanned photoacoustic microscope. *J. Biophotonics* 2020; **13**: e202000022.
- Liu C, Liao J, Chen L *et al*. The integrated high-resolution reflection-mode photoacoustic and fluorescence confocal microscopy. *Photoacoustics* 2019; **14**: 12–18.
- Jathoul AP, Laufer J, Ogunlade O *et al*. Deep *in vivo* photoacoustic imaging of mammalian tissues using a tyrosinase-based genetic reporter. *Nat Photonics* 2015; **9**: 239–246.
- Hindelang B, Aguirre J, Schwarz M *et al*. Non-invasive imaging in dermatology and the unique potential of raster-scan optoacoustic mesoscopy. *J Eur Acad Dermatol Venereol* 2019; **33**: 1051–1061.
- Cheng Z, Ma H, Wang Z, Yang S. *In vivo* volumetric monitoring of revascularization of traumatized skin using extended depth-of-field photoacoustic microscopy. *Front Optoelectron* 2020; **13**: 307–317.
- Wu Z, Duan F, Zhang J *et al*. *In vivo* dual-scale photoacoustic surveillance and assessment of burn healing. *Biomed Opt Express* 2019; **10**: 3425–3433.
- Genina EA, Surkov YI, Serebryakova IA *et al*. Rapid ultrasound optical clearing of human light and dark skin. *IEEE Trans Med Imaging* 2020; **39**: 3198–3206.
- Wang Z, Yang F, Ma H *et al*. Photoacoustic and ultrasound (PAUS) dermoscope with high sensitivity and penetration depth by using a bimorph transducer. *J Biophotonics* 2020; **13**: e202000145.
- Aguirre J, Schwarz M, Garzorz N *et al*. Precision assessment of label-free psoriasis biomarkers with ultra-broadband optoacoustic mesoscopy. *Nat Biomed Eng* 2017; **1**: 1–8.
- Ma H, Yang S, Cheng Z *et al*. Photoacoustic confocal dermoscope with a waterless coupling and impedance matching opto-sono probe. *Opt Lett* 2017; **42**: 2342–2345.
- Xu D, Yang S, Wang Y *et al*. Noninvasive and high-resolving photoacoustic dermoscopy of human skin. *Biomed Opt Express* 2016; **7**: 2095–2102.
- Yew YW, Unnimadhava Kurup Soudamini Amma D, Kuan AHY *et al*. Raster-scanning optoacoustic mesoscopy imaging as an objective disease severity tool in atopic dermatitis patients. *J Am Acad Dermatol* 2021; **84**: 1121–1123.
- Wang LV. Multiscale photoacoustic microscopy and computed tomography. *Nat Photonics* 2009; **3**: 503–509.



- 29 Yuan Z, Jiang H. Quantitative photoacoustic tomography: recovery of optical absorption coefficient maps of heterogeneous media. *Appl Phys Lett* 2006; **88**: 231101.
- 30 Nandy S, Mostafa A, Hagemann IS *et al.* Evaluation of ovarian cancer: initial application of coregistered photoacoustic tomography and US. *Radiology* 2018; **289**: 740–747.
- 31 Bashkatov AN, Genina EA, Kochubey VI *et al.* Optical properties of human skin, subcutaneous and mucous tissues in the wavelength range from 400 to 2000 nm. *J Phys D Appl Phys* 2005; **38**: 2543.
- 32 Jonasson H, Fredriksson I, Bergstrand S *et al.* *In vivo* characterization of light scattering properties of human skin in the 475-to 850-nm wavelength range in a Swedish cohort. *J Biomed Opt* 2018; **23**: 121608.
- 33 Beard P. Biomedical photoacoustic imaging. *Interface Focus* 2011; **1**: 602–631.
- 34 Cheong WF, Prahl SA, Welch AJ. A review of the optical properties of biological tissues. *IEEE J Quantum Electron* 1990; **26**: 2166–2185.
- 35 Ritz J-P, Roggan A, Isbert C *et al.* Optical properties of native and coagulated porcine liver tissue between 400 and 2400 nm. *Lasers Surg Med* 2001; **29**: 205–212.
- 36 Young AR. Chromophores in human skin. *Phys Med Biol* 1997; **42**: 789.
- 37 Hai P, Yao J, Maslov KI *et al.* Near-infrared optical-resolution photoacoustic microscopy. *Opt Lett* 2014; **39**: 5192–5195.
- 38 Moothanchery M, Bi R, Kim JY *et al.* High-speed simultaneous multi-scale photoacoustic microscopy. *J Biomed Opt* 2019; **24**: 086001.
- 39 Oh J-T, Li M-L, Zhang HF *et al.* Three-dimensional imaging of skin melanoma *in vivo* by dual-wavelength photoacoustic microscopy. *J Biomed Opt* 2006; **11**: 034032.
- 40 Kang H, Lee S-W, Park S-M *et al.* Real-time functional optical-resolution photoacoustic microscopy using high-speed alternating illumination at 532 and 1064 nm. *J Biophotonics* 2018; **11**: e201700210.
- 41 Chen J, Zhang Y, Li X *et al.* Confocal visible/NIR photoacoustic microscopy of tumors with structural, functional, and nanoprobe contrasts. *Photonics Res* 2020; **8**: 1875–1880.
- 42 Periyasamy V, Das N, Sharma A *et al.* 1064 nm acoustic resolution photoacoustic microscopy. *J Biophotonics* 2019; **12**: e201800357.
- 43 Wang L, Jacques SL, Zheng L. MCML-Monte Carlo modeling of light transport in multi-layered tissues. *Comput Methods Programs Biomed* 1995; **47**: 131–146.
- 44 Laser Institute of America. American National Standard for Safe Use of Lasers ANSI Z136.1–2014. American National Standards Institute, Inc, Washington, DC, 2014.
- 45 Cheng Z, Ma H, Wang Z, Zhang W, Yang F, Yang S. Subpixel and on-line motion correction for photoacoustic dermoscopy. *IEEE J Sel Top Quant* 2021; **27**: 6800408.